

## Supporting Information

### MoS<sub>2</sub>/WS<sub>2</sub> Heterojunction for Photoelectrochemical Water Oxidation

*Federico M. Pesci<sup>1</sup>, Maria S. Sokolikova<sup>1</sup>, Chiara Grotta<sup>1</sup>, Peter C. Sherrell<sup>1</sup>, Francesco Reale<sup>1</sup>, Kanudha Sharda<sup>1</sup>, Na Ni<sup>1</sup>, Pawel Palczynski<sup>1</sup>, Cecilia Mattevi<sup>1\*</sup>*

<sup>1</sup>Imperial College London, Department of Materials, London, SW7 2AZ, UK

\* Corresponding author: c.mattevi@imperial.ac.uk

#### ToF-SIMS Characterization

Time-of-flight secondary ion monitoring mass spectrometry (ToF-SIMS) was performed on thin films (60 nm) of MoS<sub>2</sub>/WS<sub>2</sub> heterojunction films deposited on FTO coated glass using a IONTOF TOF.SIMS<sup>5</sup>-Qtac<sup>100</sup> LEIS system. Depth profiling was carried out using Cs<sup>+</sup> ion etching over a 200 μm x 200 μm area, with secondary ion monitoring on the ejected surface ions until the SnO<sup>+</sup> signal was homogeneous across the 2D plane of the examined sample.

Both 3D and 2D ToF-SIMS maps recorded for a 2H MoS<sub>2</sub>/WS<sub>2</sub> bulk heterojunction thin film on FTO demonstrated an equivalent distribution of MoS<sub>2</sub> and WS<sub>2</sub> flakes localized in the same geometric areas (Figure S1). The topographical variations visible in the 2D and 3D surface map plots of SIMS of both MoS<sub>2</sub><sup>+</sup> and WS<sub>2</sub><sup>+</sup> ions, arise due to the surface roughness of the underlying FTO glass. The lack of localization of MoS<sub>2</sub><sup>+</sup> or WS<sub>2</sub><sup>+</sup> individually provides strong evidence that there is no preferential restacking of WS<sub>2</sub> flakes with WS<sub>2</sub> or MoS<sub>2</sub> flakes with MoS<sub>2</sub> either in the exfoliated solution or during the dip coating process.

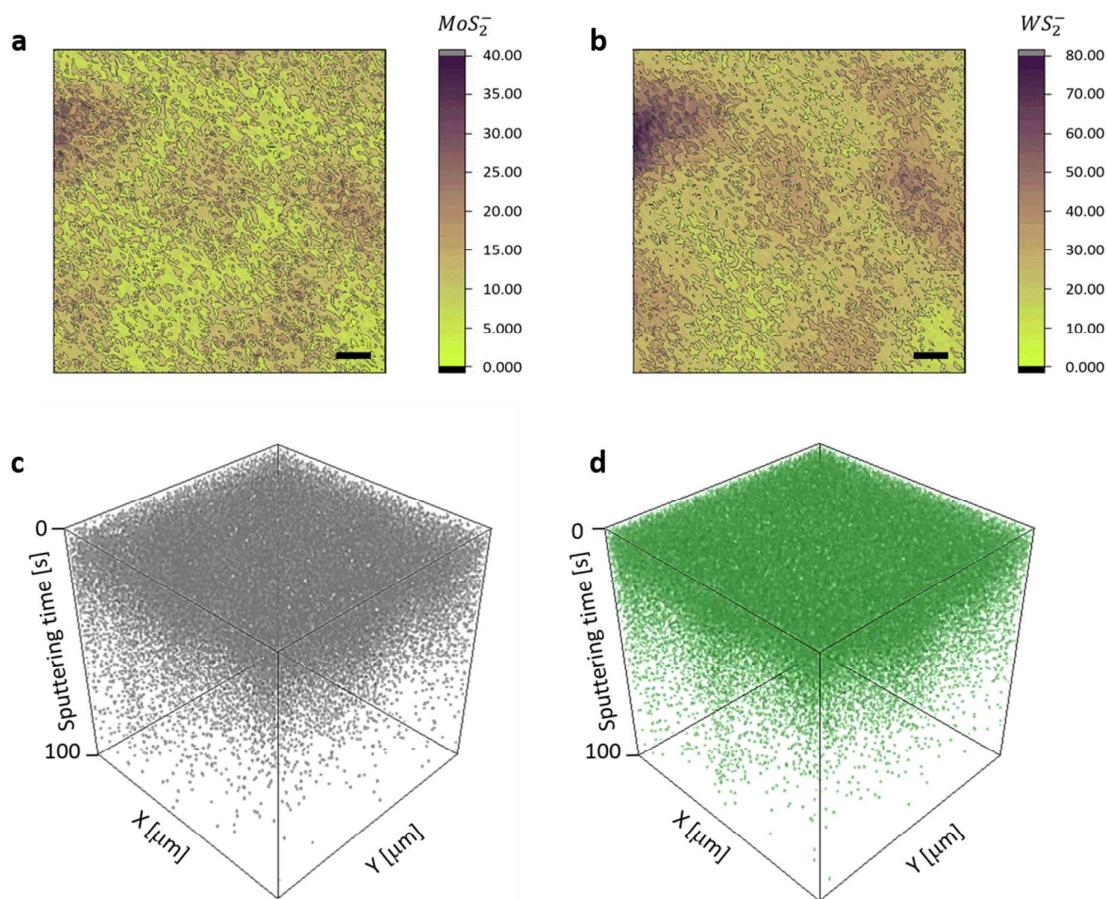


**Figure S1.** ToF-SIMS maps: a)  $\text{MoS}_2^-$  and b)  $\text{WS}_2^-$  2D ToF-SIMS maps and relative c)  $\text{MoS}_2^-$  and d)  $\text{WS}_2^-$  3D ToF-SIMS maps of a  $\text{MoS}_2/\text{WS}_2$  bulk heterojunction thin film (~60 nm) deposited on a FTO coated glass. Scale bar 10  $\mu\text{m}$ .

### X-ray diffraction (XRD) characterization

The X-ray diffraction patterns of the  $\text{WS}_2$  powder and ~60 nm thick films of exfoliated  $\text{MoS}_2$  and  $\text{WS}_2$  deposited onto glass substrates were obtained using a PANalytical XPERT-PRO X-ray diffractometer using a  $\text{Cu K}\alpha$  X-ray source. The spectra were obtained from 5-80 deg with a step size of 0.0084 deg and 21s per step.

X-ray diffractograms were recorded for thin films of restacked exfoliated  $\text{MoS}_2$  and  $\text{WS}_2$  nanosheets and  $\text{MoS}_2/\text{WS}_2$  bulk heterojunctions after annealing at 350°C in controlled

atmosphere and for MoS<sub>2</sub> and WS<sub>2</sub> bulk powders (Figure S2).

All the XRD patterns show a strong peak located at the same position as the (002) peak ( $2\theta=14.3^\circ$ ) for the bulk WS<sub>2</sub> or MoS<sub>2</sub> which indicates an interlayer spacing of 0.62 nm. Exfoliated and restacked nanosheets of MoS<sub>2</sub> and WS<sub>2</sub> present broadening, decreased intensity of the (002) peak ( $2\theta=14.2^\circ$ ) and the disappearance of all the other peaks Figure S2b, compared with bulk WS<sub>2</sub> and MoS<sub>2</sub> powders Figure S2a. This suggests that the transition metal dichalcogenides (TMDCs) sheets are exfoliated and their basal planes retain a semi-parallel orientation to the substrate.<sup>1,2</sup>

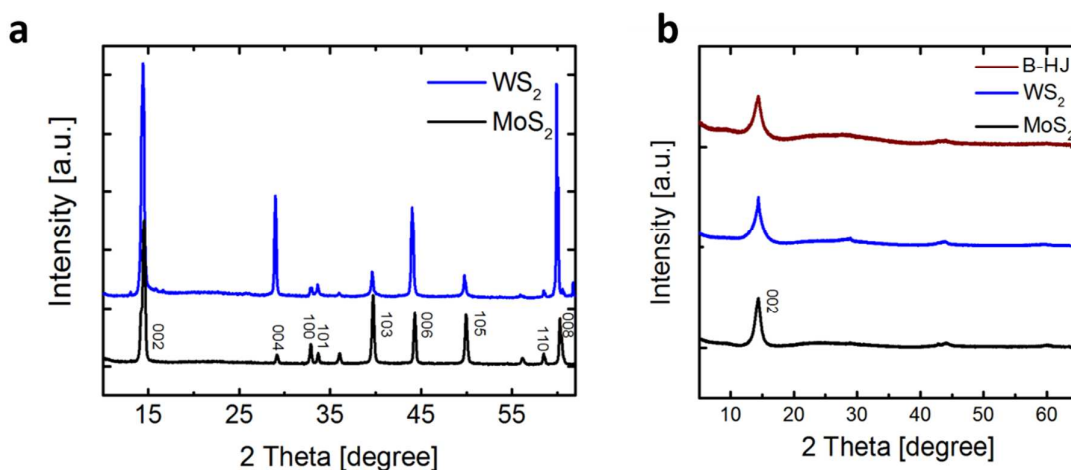


**Figure S2.** XRD patterns: a) XRD diffractograms recorded for bulk WS<sub>2</sub> (blue line) and MoS<sub>2</sub> (black line) powders and b) XRD patterns recorded for thin films (~60 nm) of MoS<sub>2</sub> (black line), WS<sub>2</sub> (blue line) and MoS<sub>2</sub>/WS<sub>2</sub> bulk heterojunctions (red line).

### Scanning Transmission Electron Microscopy (STEM) Characterisation

The STEM micrograph (Figure S3) shows the morphology of a bulk heterojunction film comprised of semi-planar restacked nanosheets of MoS<sub>2</sub> and WS<sub>2</sub> (Figure S3a) which are completely intermixed. The two constituents and the porosity are determined on the bases of the image contrast (Figure S3b), where MoS<sub>2</sub> is expressed in green, WS<sub>2</sub> in red and the

porosity in blue. TEM foils were prepared from the bulk heterojunction film by FIB milling using a Helios NanoLab 600 instrument (2-30 keV  $\text{Ga}^+$  incident beam energy with currents of 16 pA-21 nA). The specimens were FIB polished at the last stage with 5 keV and then 2 keV  $\text{Ga}^+$  to reduce the damage caused by the high energy  $\text{Ga}^+$  beam. TEM was carried out on a JEOL 2100F microscope operating at 200 kV.

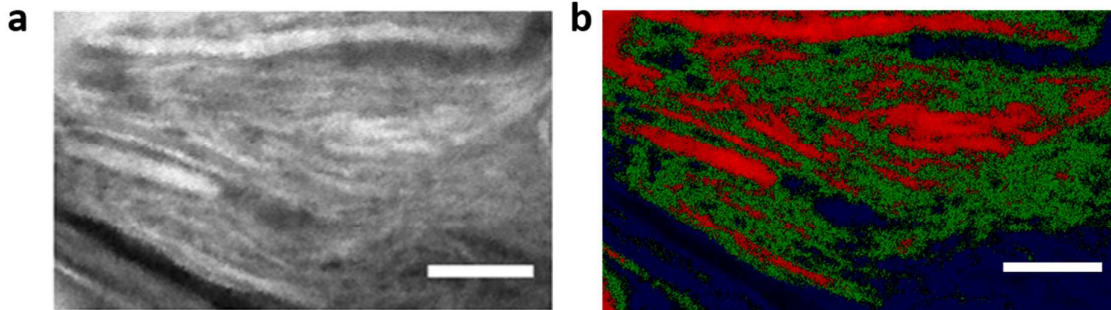


**Figure S3.** a) STEM micrograph of a MoS<sub>2</sub>/WS<sub>2</sub> bulk heterojunction film (~ 60 nm thick) deposited on FTO glass b) false color STEM micrograph highlighting MoS<sub>2</sub> (green), WS<sub>2</sub> (red) and porosity (blue). (Scale bar 20 nm).

#### UV-Vis spectra of 1T and 2H thin films of MoS<sub>2</sub> and WS<sub>2</sub>

The UV-Vis spectra recorded prior and after annealing of the thin films confirm the fact that there is a transition between metallic 1T and semiconducting 2H phase for both MoS<sub>2</sub> and WS<sub>2</sub> (Figure S4).

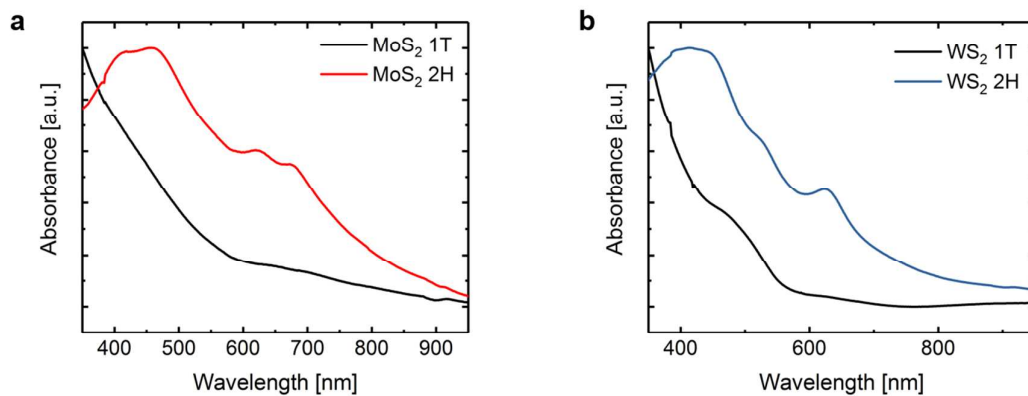


**Figure S4.** UV-Vis spectra of 1T and 2H thin films (~60nm) of a) MoS<sub>2</sub> and b) WS<sub>2</sub>.

## Raman Spectroscopy maps

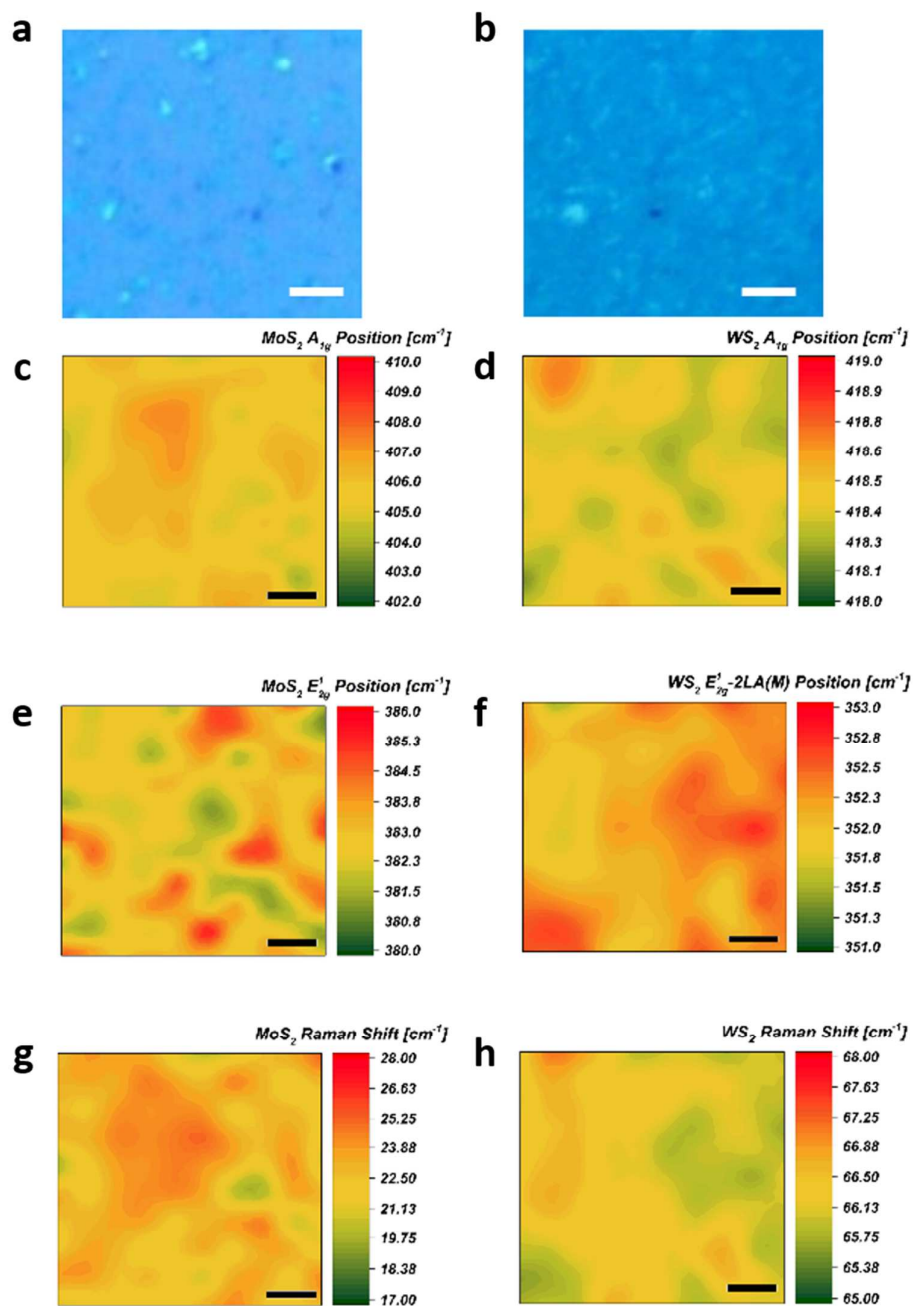


**Figure S5.** Raman spectroscopy maps over a  $10 \times 10 \mu\text{m}$  area of  $\sim 60 \text{ nm}$  thick  $\text{MoS}_2$  and  $\text{WS}_2$  films: a) optical micrographs of the selected  $10 \times 10 \mu\text{m}$  areas of  $\sim 60 \text{ nm}$  thick  $\text{MoS}_2$  film and b)  $\text{WS}_2$  film, scale bar  $2 \mu\text{m}$ ; c)  $A_{1g}$  frequency mode for  $\text{MoS}_2$  and d)  $\text{WS}_2$ , scale bar  $2 \mu\text{m}$ ; e)

$E_{1g}^1$ -2LA(M) frequency mode for MoS<sub>2</sub> and f) WS<sub>2</sub>, scale bar 2  $\mu$ m; g) frequency difference between the  $E_{1g}^1$  and the  $A_{1g}$  frequencies for MoS<sub>2</sub> and h) frequency difference between the  $E_{2g}^1$ -2LA(M) and the  $A_{1g}$  frequencies for WS<sub>2</sub>. The excitation wavelength is 532 nm. Scale bar 2  $\mu$ m.

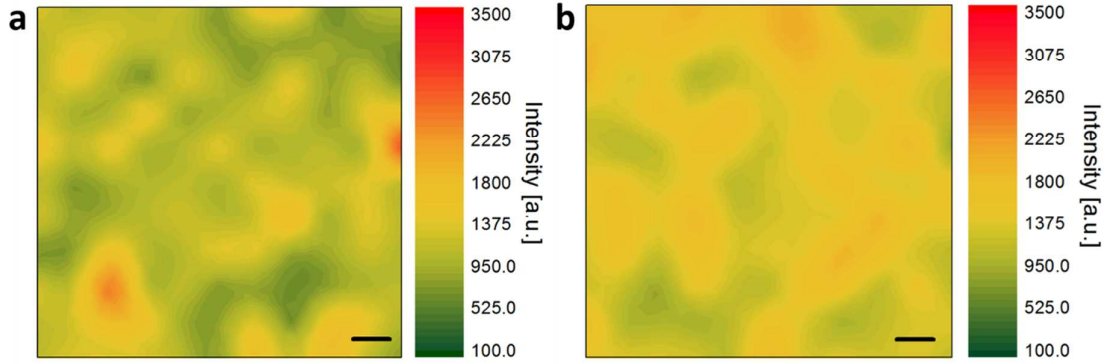


**Figure S6.**  $A_{1g}$  Raman mode intensity maps over a 10x10  $\mu$ m area of a  $\sim$  60 nm thick B-HJ film: a) MoS<sub>2</sub> and b) WS<sub>2</sub>. The excitation wavelength is 532 nm. Scale bar 1  $\mu$ m.

### UV-Vis absorption

UV-Vis spectra of thin films ( $\sim$  60 nm) of MoS<sub>2</sub> and WS<sub>2</sub> deposited on fused silica substrates were fitted using a combination of Lorentzian functions taking in account the scattering due to the thickness of the films (Figure S7).

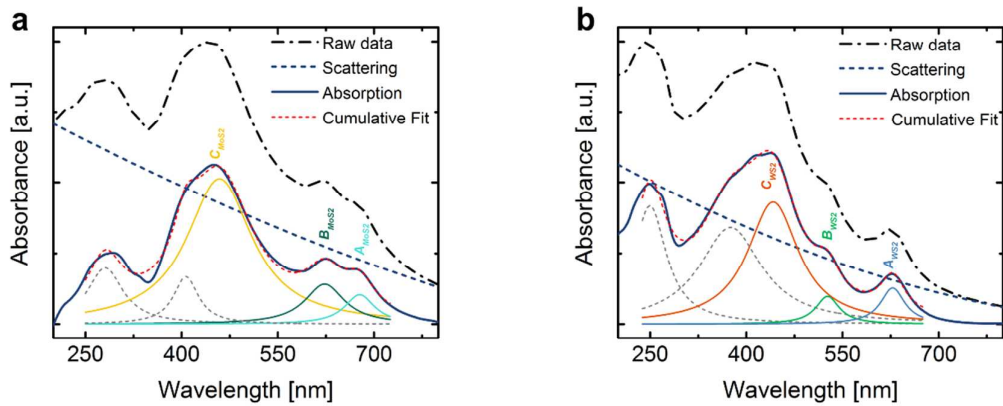




**Figure S7.** UV-Vis absorption spectra: UV-Vis spectra recorded between 200 and 1000 nm for thin films ( $\sim 60$  nm) of a) MoS<sub>2</sub> and b) WS<sub>2</sub>. The spectra were fitted with a combination of Lorentzian functions after being corrected to the scattering arising from the film thickness.

### Photoluminescence spectra and maps

Spatial maps of PL intensity and peak position (eV) of WS<sub>2</sub> and MoS<sub>2</sub> films (Figure S8) are largely uniform across the entire film area. The uncertainties of the peak position reported in the main text are the standard errors.

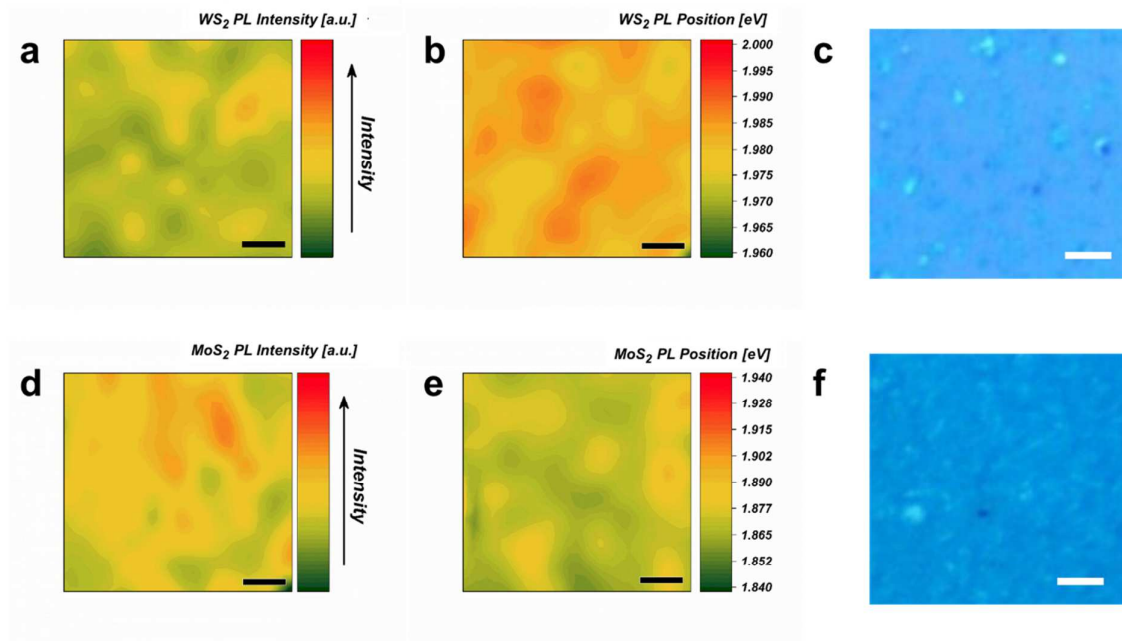


**Figure S8.** Photoluminescence maps: photoluminescence intensity maps (a,d), peak position (eV) maps (b,e) and relative optical micrographs (c,f), for a  $10 \times 10 \mu\text{m}$  region of  $\sim 60$  nm thick WS<sub>2</sub> (top) and a MoS<sub>2</sub> (bottom) films. The excitation wavelength is 532 nm. Scale bar  $2 \mu\text{m}$ .

### Electrical measurements

Electrical measurements were carried out in a two probe configuration for space-charge-limited-current (SCLC) devices prepared from thin films ( $\sim 2 \mu\text{m}$ ) of  $\text{MoS}_2$  nanosheets,  $\text{WS}_2$  nanosheets and  $\text{MoS}_2/\text{WS}_2$  bulk heterojunctions (Figure S9). The TMDC materials were deposited on top of a thin layer of  $\text{TiO}_2$  ( $\sim 15 \text{ nm}$ ) in a  $\text{FTO}/\text{TiO}_2/\text{TMDC}/\text{Al}$  configuration where  $\text{TiO}_2$  was employed as a hole blocking layer to confirm that under positive voltage the materials exhibit electron transport.

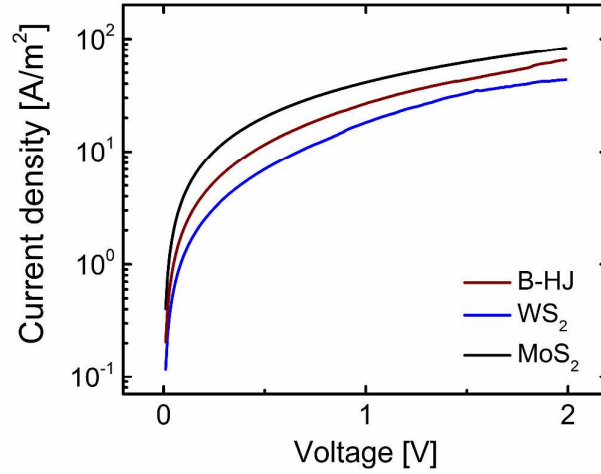


**Figure S9.** J-V curves for the SCLC devices: current density Vs. voltage curves recorded for  $\text{MoS}_2$  (black line),  $\text{WS}_2$  (blue line) and  $\text{MoS}_2/\text{WS}_2$  bulk heterojunction (red line) films.

From the fitting of the  $J$ - $V^2$  curves with the Mott-Gurney equation (Equation E1) it was possible to extract the electron mobility across the film for the three devices.

$$J = \frac{\mu \epsilon \epsilon_0 9V^2}{8d^3} \quad \text{Equation E1}$$



Where  $\mu$  is the electron mobility, the dielectric constant  $\epsilon$  of the TMDC,  $\epsilon_0$  the vacuum permittivity and  $d$  the thickness of the films. The dielectric constant for MoS<sub>2</sub>, WS<sub>2</sub> and MoS<sub>2</sub>/WS<sub>2</sub> heterojunctions were considered to be 4.8, 4.4 and 4.6 respectively.<sup>3</sup> The extracted mobilities were  $3.41 \times 10^{-2}$ ,  $2.37 \times 10^{-2}$  and  $3.91 \times 10^{-2} \text{ cm}^2 \text{ V}^{-1} \text{ s}^{-1}$  for MoS<sub>2</sub>, WS<sub>2</sub> and MoS<sub>2</sub>/WS<sub>2</sub> heterojunctions respectively.

### X-Ray photoelectron spectroscopy characterization

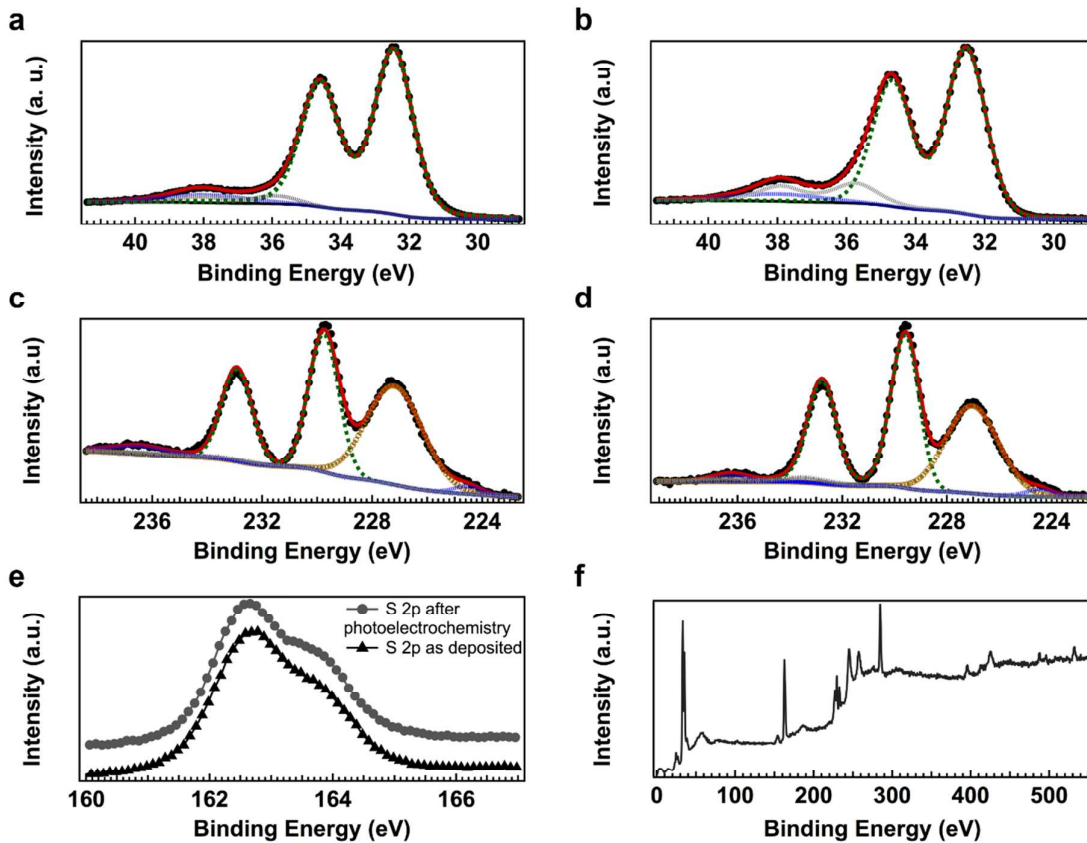


**Figure S10:** XPS spectra of the W 5p and W 4f core level peak regions a) before and b) after photo electrochemical characterization; the Mo 2s and Mo 3d core level peak regions c) before and d) after photo electrochemical characterization and the e) S 2p core levels before and after photoelectrochemical measurements. The spectra have been collected for a  $\sim 60 \text{ nm}$  thick film of B-HJ onto FTO. An extended spectrum f) shows the presence of WS<sub>2</sub> and MoS<sub>2</sub>

in 50:50 at. % and weak core level peaks related FTO. The spectra were fit by Doniach-Sunjjic function after subtracting a Shirley background (black line).

We studied the chemical composition of B-HJ films ~ 60 nm thick deposited onto FTO before and after photoelectrochemical measurements by in situ X-Ray photoelectron spectroscopy (XPS). XPS spectra of the experimental data (reported as black dots) showing the W4f, Mo 3d and S 2p peaks regions are reported in Figure S10. W 4f<sub>7/2</sub> and 5/2 core levels were fit (green line) and the resulting peaks are centered at 32.9 eV and 35.1 eV respectively in agreement with W<sup>4+</sup> in 2H-WS<sub>2</sub>. To fully fit the entire spectral region, the W 5p core level was identified at 38.5 eV (blue line) and two nearly negligible components of 4f W<sup>6+</sup> attributable to W-O bonds (likely to be in the form of WO<sub>3</sub>)<sup>4</sup> centered at 36.2 eV and 38.5 eV respectively (grey line). The W-O bonds are likely to be present at the edges of the flakes as a consequence of air exposure of the material.<sup>5-7</sup>

The W 4f core levels present the same intensity before and after photoelectrochemical measurements suggesting a good stability of the material. A small increase of the W-O bonds has been detected after extensive photoelectrochemical testing. This is probably due to further oxidation of the edges of flakes lying inside the films which are accessible to water via the intrinsic porosity of the film.

The Mo 3d 5/2 and 3/2 core levels are fit (green line) and they are centered at 229.6 eV and 232.8 eV respectively and thus attributable to Mo<sup>4+</sup> in 2H-MoS<sub>2</sub>. Two negligible components of Mo 3d 5/2 and 3/2 centered at 233.3 eV and 236.2 eV (grey line) respectively were identified and are ascribable to Mo-O bonds (Mo<sup>6+</sup>)<sup>5-7</sup> which are likely to be present at the edges of the flakes as a consequence of air exposure of the material.

Similarly, to the W<sup>4+</sup> core levels, Mo<sup>4+</sup> core levels do not show any change before and after photoelectrochemical testing (Figure S10 c and d) while the Mo-O components present a

nearly negligible increase. The peak at 227 eV is due to the S 2s core level (yellow line) while the two small peaks at 224.4 eV (blue line) and at 236.4 eV (blue line) are two satellite peaks due to Mo 3d 3/2 and W 4f 5/2 respectively, excited by the Mg K $\alpha$ 2 incident radiation. Overall, W 4f and Mo 3d components related to W-O and Mo-O respectively, are close to the background level and comparable to what observed in thin films of exfoliated TMDCs reported before.<sup>4,8-10</sup>. Their presence can be attributed to oxidation of the edges of the flakes due to exposure to air which can slightly increase after photoelectrochemical measurements. Overall, the materials do not present any extensive oxidation/degradation.

The S 2p $_{3/2}$  and 1/2 core levels are indistinguishable before and after photoelectrochemical measurements suggesting that we can exclude the formation of any oxysulfide species or loss of sulfur. An extended XPS spectrum which includes all the core levels of W, Mo and S has been collected to calculate the atomic percentage of WS<sub>2</sub> and MoS<sub>2</sub> which has been confirmed to be 50:50 atomic % as expected on the basis of the molar ratio of the two materials utilized for the chemical exfoliation.

Photoemission spectra were acquired on a custom designed ultra-high-vacuum UHV system, working at a base pressure of 10<sup>-10</sup> mbar, equipped with a VG MK II Escalab electron analyser. Core level photoemission spectra (XPS) were recorded at RT in normal emission using a non-monochromatized Mg K $\alpha$  X-ray source (1253.6 eV). The spectrometer energy calibration was carried out by using a gold sample (Au 4f at 84 eV). Single spectral regions were collected using 0.1 eV steps, 0.5 s collection time and 20 eV pass energy.

### **Chronoamperometry recorded under continuous irradiation.**

The stability of the B-HJ electrodes have also been confirmed by relatively long chronoamperometry scans under continuous irradiation (Figure S11). It can be noted that when the photoanode is exposed to white light a stable photocurrent is generated, indicating

good stability of the film under operational conditions. The photocurrent recorded under the application of a positive bias during oxygen evolution measurements was employed to calculate the faradic efficiency of the photoanodes.

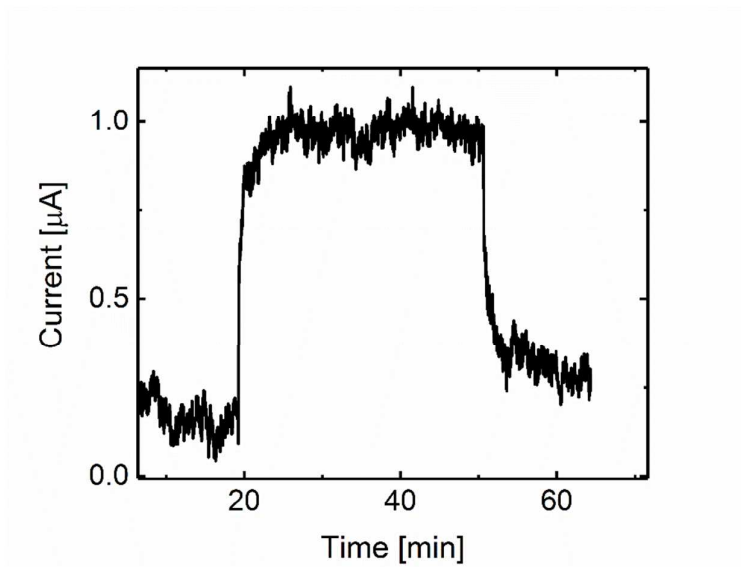


**Figure S11.** Chronoamperometry recorded for a thin (~60 nm) B-HJ film kept under a positive applied bias (+1V vs RHE) and under white light irradiation ( $100 \text{ mW cm}^{-2}$ ).

#### **Possible role of $\text{WO}_3$ in IPCE measurements.**

To rule out any possible contribution of oxidized  $\text{WS}_2$  in the form of  $\text{WO}_3$  to the IPCE recorded for the B-HJ electrode, a 60 nm film of  $\text{WS}_2$  deposited on FTO doped glass was annealed in air at  $350^\circ\text{C}$  for two hours in order to induce oxidation of  $\text{WS}_2$  and thus formation of  $\text{WO}_3$ . The oxidation was confirmed by XRD characterization (Figure S12a). A strong attenuation of the  $\text{WS}_2$  (002) peak and the appearance of characteristic peaks of  $\text{WO}_3$  [(110) and (220)] in its monoclinic phase (Figure S12a) are visible in the XRD pattern. The absorption spectrum of the oxidized photoanode (Figure S12b) shows a broadening of the A and B excitons peaks of  $\text{WS}_2$  and a significant increase of the absorption at wavelength lower than 400 nm indicating a strong contribution from  $\text{WO}_3$ . The IPCE recorded for the oxidized

film show a great enhancement in the UV region (Figure S12c) whereas it is almost 0% in the visible region (Figure S12c, inset), confirming that the IPCEs observed in the visible region is solely due to  $\text{WS}_2$ .

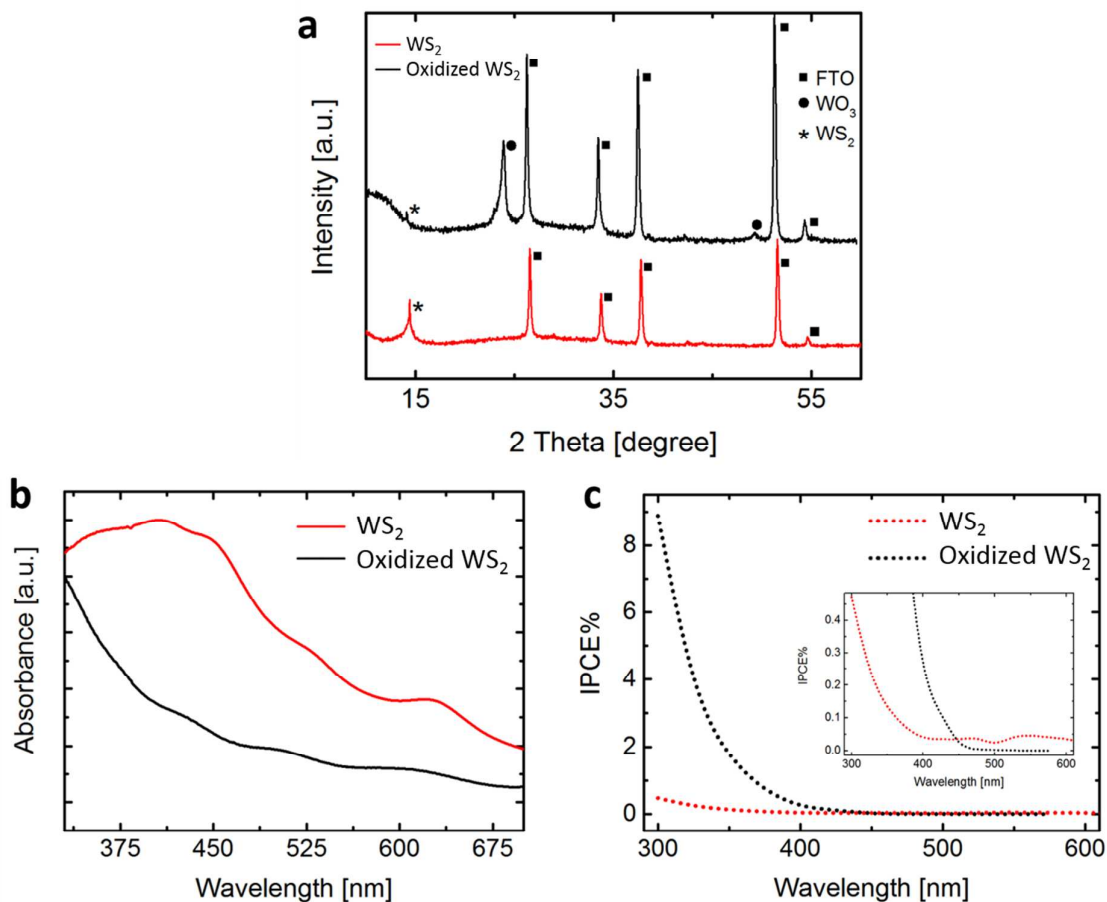


**Figure S12.** a) XRD diffraction patterns, b) UV-Vis absorption spectra and c) IPCE% spectra of a  $\sim 60\text{nm}$  thick  $\text{WS}_2$  electrode before (red line) and after (black line, “Oxidized  $\text{WS}_2$ ”) oxidation in air at  $350^\circ\text{C}$ .

### Chemical and photochemical stability of B-HJ electrodes

UV-Vis spectra for B-HJ electrodes were recorded before and after one hour of photoelectrochemical characterization under chopped simulated solar radiation (1sun, 100

$\text{mW cm}^{-2}$ ). The spectra do not show any significant change in the optical features suggesting good chemical and photoelectrochemical stability of both  $\text{MoS}_2$  and  $\text{WS}_2$  (Figure S13).

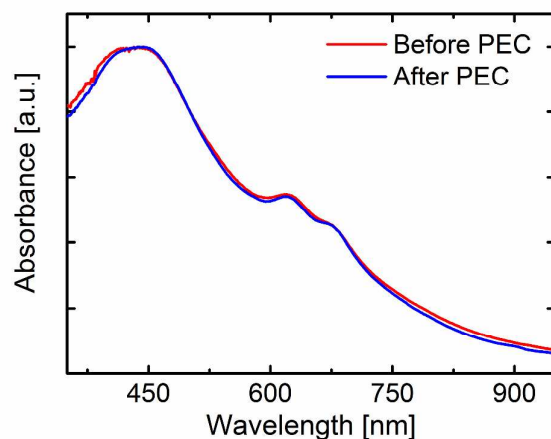


**Figure S13.** UV-Vis spectra recorded before and after photoelectrochemical characterization: UV-Vis spectra recorded for a B-HJ thin film ( $\sim 60$  nm) before and after one hour of photoelectrochemical characterization.

#### **Chronoamperometry scans of front vs back illumination for $\text{MoS}_2/\text{WS}_2$ bulk heterojunction photoanodes**

Linear sweep voltammetry and chronoamperometry were recorded for  $\text{MoS}_2/\text{WS}_2$  bulk heterojunction photoanodes by exposing the front and the back of the electrode to the incident light. Not significant current differences were observed, indicating that electron transport through the films does not affect the photocurrent (Figure S14).



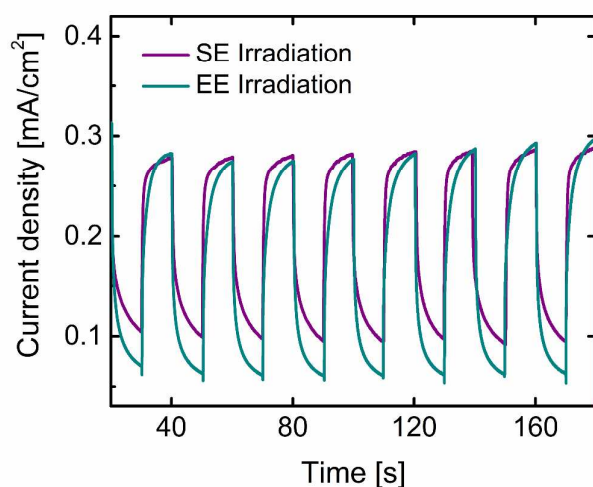


**Figure S14.** Chronoamperometry scans of front vs back illumination: chronoamperometry curves recorded for a  $\sim 60$  nm thick B-HJ photoanode from the back side (SE irradiation, violet line) and from the front side (EE irradiation, cyan line).

#### **Incident-Photon-to-Current Efficiencies (IPCE) recorded for films of different thickness.**

IPCE was recorded for photoanodes of different thicknesses. The IPCE of  $\text{MoS}_2$ ,  $\text{WS}_2$  and BHJ films of different thickness from  $\sim 40$  nm to  $\sim 80$  nm are compared. In Figure S14a the IPCE of 40 nm films of the three electrode materials are reported. Similarly, the IPCE of  $\sim 60$  nm and  $\sim 80$  nm films of the three electrode materials are reported in Figure S14b and c. The IPCE of the BHJ is constantly the highest across the whole visible range, followed by  $\text{WS}_2$  and  $\text{MoS}_2$ . The IPCE increases with the thickness of the B-HJ films indicating that the amount of light absorbed is a determining factor for efficiency (Figure S15d). The fact that the IPCE recorded for the  $\sim 40$  nm B-HJ electrode does not fully reflect the absorption spectrum of the materials is due to the experimental uncertainty arising from the small photocurrents recorded under irradiation.

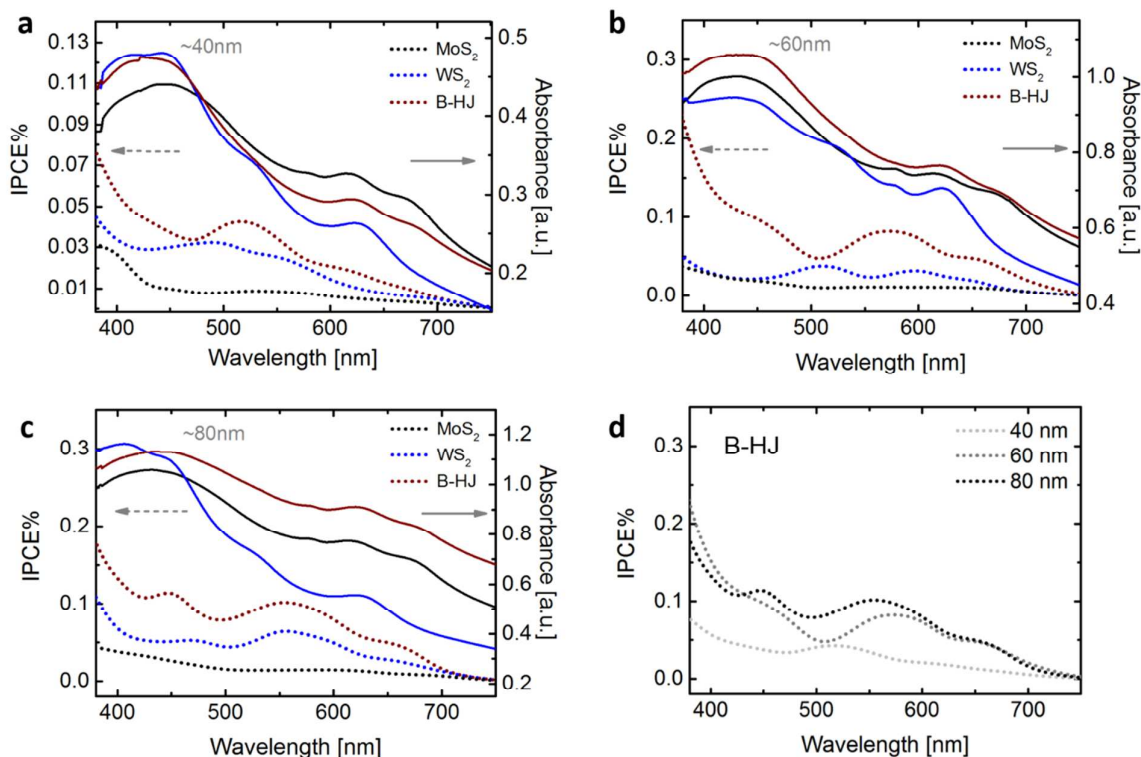


**Figure S15.** Incident-photon-to-current efficiency (%) curves measured in the range from 380 nm to 750 nm of incident light for B-HJ (red dots), WS<sub>2</sub> (blue dots) and MoS<sub>2</sub> (black dots) thin films with different thicknesses: a) ~ 40 nm; b) ~ 60 nm and c) ~ 80 nm. The IPCE (%) of B-HJ films of different thicknesses are reported also in panel d) for direct comparison.

### Incident-Photon-to-Current Efficiencies (IPCE) for planar heterojunctions

IPCE was recorded for planar heterojunctions consisting of FTO/WS<sub>2</sub>/MoS<sub>2</sub> and FTO/MoS<sub>2</sub>/WS<sub>2</sub> formed by ~ 30 nm thick films of each constituent. Planar heterojunctions of FTO/MoS<sub>2</sub>/WS<sub>2</sub> show lower IPCE (~ 0.014% at 600 nm, Figure S16) than bulk heterojunctions (~ 0.09% at 600 nm, Figure S15b), however this is higher than the individual constituents IPCE. This is likely to be due to the limited interfacial area between MoS<sub>2</sub> and

WS<sub>2</sub> compared to the bulk heterojunction. The inverted planar heterojunction, namely FTO/WS<sub>2</sub>/MoS<sub>2</sub> also manifests lower IPCE than the bulk heterojunction and comparable to exfoliated WS<sub>2</sub> thin films.

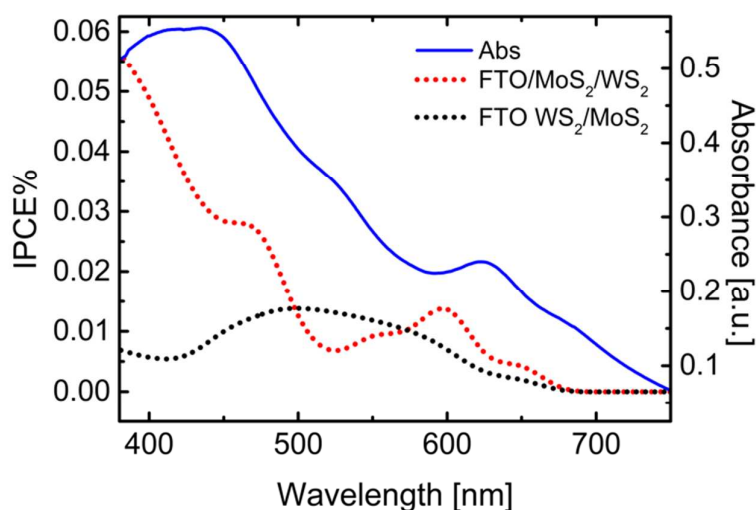


**Figure S16.** IPCE of planar heterojunction electrodes: UV-Vis spectrum (blue line) and IPCE recorded for a FTO/MoS<sub>2</sub>/WS<sub>2</sub> planar heterojunction photoanode (red dots) and a FTO/WS<sub>2</sub>/MoS<sub>2</sub> planar heterojunction photoanode (black dots). All the films investigated are ~ 60 nm thick.

## Bibliography

- (1) Qin, X. R.; Yang, D.; Frindt, R. F.; Irwin, J. C. *Ultramicroscopy* **1992**, 42–44, 630–636.
- (2) Gee, M. A.; Frindt, R. F.; Joensen, P.; Morrison, S. R. *Mater. Res. Bull.* **1986**, 21, 543–549.
- (3) Chang, J.; Register, L. F.; Banerjee, S. K. *J. Appl. Phys.* **2014**, 115, 84506.
- (4) Mohamad Latiff, N.; Wang, L.; Mayorga-Martinez, C. C.; Sofer, Z.; Fisher, A. C.; Pumera, M. *Nanoscale* **2016**, 8, 16752–16760.

- (5) Cattelan, M.; Markman, B.; Lucchini, G.; Das, P. K.; Vobornik, I.; Robinson, J. A.; Agnoli, S.; Granozzi, G. *Chem. Mater.* **2015**, *27*, 4105–4113.
- (6) Martinez, H.; Benayad, A.; Gonbeau, D.; Vinatier, P.; Pecquenard, B.; Levasseur, A. *Appl. Surf. Sci.* **2004**, *236*, 377–386.
- (7) Dupin, J. C.; Gonbeau, D.; Martin-Litas, I.; Vinatier, P.; Levasseur, A. *Appl. Surf. Sci.* **2001**, *173*, 140–150.
- (8) Voiry, D.; Yamaguchi, H.; Li, J.; Silva, R.; Alves, D. C. B.; Fujita, T.; Chen, M.; Asefa, T.; Shenoy, V. B.; Eda, G.; Chhowalla, M. *Nat. Mater.* **2013**, *12*, 850–855.
- (9) Wang, H.; Kong, D.; Johanes, P.; Cha, J. J.; Zheng, G.; Yan, K.; Liu, N.; Cui, Y. *Nano Lett.* **2013**, *13*, 3426–3433.
- (10) Yu, X.; Prévot, M. S.; Guijarro, N.; Sivula, K. *Nat. Commun.* **2015**, *6*, 7596–7603.